First-principles study of the thermodynamic and vibrational properties of ReS_2 under pressure

Natalya Sheremetyeva,[1] Damien Tristant,[1] Anthony Yoshimura,[1]
Jason Gray,[1] Liangbo Liang,[2] and Vincent Meunier[1,*]
[1]*Department of Physics, Applied Physics, and Astronomy, Rensselaer Polytechnic Institute, Troy, New York 12180, USA*
[2]*Center for Nanophase Materials Sciences, Oak Ridge National Laboratory, Oak Ridge, Tennessee 37830, USA*

(Received 18 September 2019; published 3 December 2019)

Density functional theory is used to investigate the effect of hydrostatic pressure on the structural, energetic, electronic, and vibrational properties of bulk ReS_2. The phase transition from the distorted $1T$ phase to the high-pressure distorted $1T'$ phase is rationalized based on the evaluation of their thermodynamic potentials. The electronic band gap of the $1T$ phase is shown to undergo a nearly direct to indirect transition at about 9 GPa, while the $1T'$ phase is found to remain a robust nearly direct band-gap material under pressure. The computational analysis of the vibrational properties of both ReS_2 phases reproduces existing experimental Raman spectroscopy data for ω vs P trends and provides a path towards an accurate phase discrimination using infrared spectroscopy, inelastic neutron, and x-ray scattering.

DOI: 10.1103/PhysRevB.100.214101

I. INTRODUCTION

Layered transition-metal dichalcogenides (TMDs) form an emerging class of two-dimensional materials (2DMs) beyond graphene and have been studied with increasing interest recently [1–8]. Typical TMDs have the general formula MX_2, where M stands for a transition-metal atom like, e.g., Mo, W, or Re, and X denotes a chalcogen atom like S, Se, or Te. Many interesting properties have been demonstrated in these materials, like charge-density waves [9–11] and superconductivity [12–14], making 2DMs promising candidates for novel applications.

Among the prominently studied TMDs, ReS_2 stands out due to its relatively weak interlayer coupling, resulting in layer thickness independent vibrational, optical, and electronic properties. One attractive consequence is that ReS_2 is a direct band-gap semiconductor in both its monolayer and bulk forms [13], in contrast to other broadly studied group-IV TMDs such as MoS_2 which exhibit a indirect-to-direct band-gap transition when thinned down from bulk to monolayer. ReS_2 is also distinct in that it exists most commonly in a distorted $1T$ phase, as opposed to the more symmetric $1T$, $1H$, $2H$, and $3R$ structures assumed by most of the other TMDs. This results in electronic [15] and optical [16] anisotropy that can be utilized in the design of nanoscale devices, including polarization-sensitive light detectors [16] and logic gates composed of anisotropic field-effect transistors [17]. The reduced symmetry has also been shown to induce spontaneous vertical growth on a variety of substrates [18], allowing for abundant access to edge adsorption sites, which could facilitate the use of ReS_2 in catalysis and reaction engineering.

The very weak interlayer coupling in bulk ReS_2 is responsible for its unique properties, and potentially allows for its usage as a 2D material without the need of the more challenging preparation of large-scale monolayers [13]. However, the layer decoupling is also what makes understanding the interlayer interactions in this material so elusive. Such understanding is important for controlling and designing novel materials with similar properties. Moreover, the original report of the direct nature of bulk ReS_2's band gap was contested by subsequent experimental [19,20] and theoretical [21,22] studies. The current consensus is that ReS_2 has almost degenerate indirect (1.41 eV) and direct (1.5 eV) band gaps [23].

Application of high external pressure has been widely used as a method for modifying the properties of 2DMs [24–28]. In bulk MoS_2, for example, an electronic transition from a semiconducting to metallic state was reported at ∼19 GPa and was linked to the pressure-induced lattice distortion [29]. Analogous pressure-induced semiconductor-to-metal transitions have also been reported in $MoSe_2$ [30], WS_2 [26,31], and VS_2 [32].

Specifically in bulk ReS_2, application of external pressure has been used as a way to modify the interlayer interactions and the resulting material properties [13,23,33–35]. Several structural phase transitions occur in ReS_2 under the effect of pressure with the first one taking place at about 8–11 GPa [23,33,34,36]. Electronic properties change with pressure as well. The electronic band gap decreases with increasing pressure all the way to complete metallization at about 70 GPa [23,33,34]. For this reason, exact knowledge of and control over the pressure at which the first phase transition occurs is desirable. However, to date, a thorough characterization of the first high-pressure phase is not yet completed.

First-principles calculations based on density-functional theory (DFT) have greatly aided experimental studies in understanding the pressure dependence of various properties of ReS_2 [23,33–35]. Specifically, DFT simulations revealed the lattice parameters of the first high-pressure phase denoted as distorted $1T'$ [33,34]. The ambient and the high-pressure phases are structurally very similar as they differ mainly in the details of their layer stacking configuration. This explains

*meuniv@rpi.edu

why the experimental distinction between the two phases is a challenging task. Furthermore, DFT calculations to date have not been able to resolve the ambiguity regarding the phase-transition pressure as different exchange-correlation functionals used in DFT can yield different results [33,34]. In addition, temperature effects on the energetic differences between the two phases have not been considered.

Raman spectroscopy has been successfully employed for high-precision characterization of 2D layered materials [37]. This nondestructive technique is known to be especially sensitive to structural features, like layer number and stacking order. The vibrational properties of ambient ReS_2 accessible by Raman spectroscopy have been previously studied experimentally and theoretically [38–40]. Owing to the low symmetry of its unit cell, ReS_2 exhibits many more nondegenerate modes in its Raman spectrum compared to traditional TMDs. Similarly, the associated vibrational modes feature more complicated patterns [38]. The pressure dependence of Raman-active phonon frequencies has been studied experimentally and used for phase-transition detection [13,23,34], but these studies focused on the high-frequency intralayer modes, instead of the low-frequency interlayer phonon modes that can more effectively probe the weak interlayer coupling and stacking patterns in 2D materials [37]. Note that due to the unit cell of bulk ReS_2 consisting of a single layer, low-frequency interlayer modes are unfortunately Raman inactive and cannot be accessed by Raman spectroscopy, but they can be accessed in other vibrational spectroscopies such as neutron scattering.

In this work, we used DFT to systematically characterize both the ambient and high-pressure phases of bulk ReS_2. This study focuses on energetic, electronic, and vibrational properties under the effect of pressure up to 15 GPa. We provide an atomistic description of the phase transition from the distorted $1T$ to $1T'$ phase using the thermodynamic potentials. The electronic band gaps of the $1T$ and $1T'$ phases are found to exhibit contrasting dependence on pressure. Our study of phonons highlights the role vibrational spectroscopy (e.g., Raman, infrared, neutron, and x-ray scattering) can have in providing an unambiguous discrimination between the $1T$ and $1T'$ phases.

The rest of this paper is organized as follows. Technical details are provided in Sec. II, results are exposed in Sec. III, and a summary of the findings is given in Sec. IV.

II. METHODS

First-principles calculations based on density functional theory were carried out using the VASP package [41–43]. Electron-ion interactions were described within the projector-augmented-wave (PAW) method using a plane-wave basis set [44]. Based on careful convergence tests, a plane-wave basis energy cutoff of 600 eV was used together with a dense Γ-point centered $10 \times 10 \times 10$ k-point grid sampling. The electronic minimization tolerance was set to 10^{-8} eV and the tolerance for minimization of residual forces during relaxation of atomic positions was set to 6 meV/Å. Such stringent convergence criteria were found to be necessary to ensure that the vibrational properties are evaluated at the numerical minimum of the potential landscape, and thus to avoid the appearance of spurious imaginary frequencies.

Several approximations to the exchange-correlation functional were tested: The local density approximation (LDA) [41], the generalized gradient approximation (GGA) in the Perdew-Burke-Ernzerhof (PBE) formulation [45], PBE with corrections to describe the weak van der Waals (vdW) interactions within the optB88-vdW functional [46,47], and the meta-GGA SCAN (strongly constrained and appropriately normed) functional [48]. A comparison of lattice parameters and bulk moduli calculated with each functional and available experimental values [34,49] is provided in the Supplemental Material (SM) [50]. LDA has been successfully used to describe the lattice parameters and phonon frequencies of many layered 2D materials at ambient conditions. The success of LDA is explained in part by fortuitous cancellations of errors, since LDA does not capture the weak interlayer vdW forces but simultaneously overestimates the covalent binding between layers.

Moving beyond LDA, we found that PBE alone does not reproduce the experimentally reported bulk modulus B_0 of ReS_2. The calculated PBE B_0 is an order of magnitude smaller than the experimental value, suggesting that PBE makes the structure much easier to compress compared to experimental reports (see Table 1 in the SM [50]). The PBE + vdW functional, on the other hand, yields $B_0 = 40$ GPa and thus provides a good agreement with the experimental bulk modulus of 35 ± 5 GPa. For these reasons, the PBE + vdW functional was used throughout this work, unless stated otherwise. The meta-GGA in the SCAN formulation was tested as well. It was shown to result in very similar lattice parameters and bulk modulus as the PBE + vdW functional. Since SCAN is computationally more demanding and does not provide significant improvements over PBE + vdW in the systems of interest, it was not used in calculations of vibrational properties.

The effect of hydrostatic pressure on the structure of bulk ReS_2 was modeled by compressing the lattice according to the Birch-Murnaghan (BM) isothermal equation of state (EOS) [51,52]. The full pressure calibration procedure consists of three steps. In the first step, the energy vs volume curve is calculated for a set of arbitrary volumes at the vicinity of the equilibrium configuration. This curve is fitted to the third-order BM-EOS and the B_0 as well as its derivative B' are obtained as fitting parameters. In the second step, using the fitting parameters from step 1, the derivative $P(V) = \partial E/\partial V$ equation is solved for the volume given a desired pressure. In the last step, the equation relating the lattice constants and angles (six unknowns) to the volume from step 2 is solved for one of the lattice constants keeping all the other parameters fixed to those of the ground-state structure. The new structure obtained at the end of this procedure is then reoptimized using VASP keeping the volume of the cell constant, but allowing for the lattice shape to change during relaxation. This procedure was repeated until no change in cell volume and shape was observed. As a result of this approach, perfect hydrostatic pressure conditions are established after confirming that the diagonal elements of the stress tensor output by VASP are all equal to the desired pressure and the off-diagonal ones are essentially zero.

For each pressure value, the vibrational properties (phonon frequencies and eigenvectors) were calculated within the finite-displacement method (FDM) in the harmonic approximation using the PHONOPY package [53]. In this method, atoms are systematically displaced from their equilibrium positions and the restoring forces are calculated using VASP as given by the Hellmann-Feynman forces. From the calculated forces, interatomic force constants are determined that form the dynamical (Hessian) matrix. Diagonalization of the dynamical matrix supplies the phonon eigenfrequencies ω_j and their associated eigenvectors $\vec{e}_j$. To calculate phonons, a $3 \times 3 \times 3$ supercell of the bulk ReS_2 unit cell was used to avoid nonphysical interactions between periodic images [54]. The atomic displacement magnitude for forces calculations was set to 0.03 Å.

With the knowledge of the vibrational properties, thermodynamic quantities can be calculated. Specifically, the Gibbs free energy was evaluated in order to access the energetics of the phase transition between the ambient and high-pressure structures of ReS_2. The Gibbs free energy $G(P, T) = F(P, T) + PV$ contains additional vibrational contributions to the enthalpy captured in the free energy $F(P, T)$ term. The free energy $F(P, T)$ of the system is given by [55–57]

$$F(P,T) = \frac{1}{N}\left\{ E_{\text{cell}}(P) + \frac{1}{2}\sum_{\vec{q}\in \text{BZ},j} \hbar\omega_{\vec{q},j}(P) + k_B T \sum_{\vec{q}\in \text{BZ},j} \ln\left[1 - \exp\left(-\frac{\hbar\omega_{\vec{q}j}(P)}{k_B T}\right)\right]\right\}, \quad (1)$$

where N is the number of atoms in the cell, and $\hbar$ and k_B are the reduced Planck and the Boltzmann constants, respectively. The first term is the ground-state energy of the structure at a given pressure [and thus volume, since $P(V)$]. The next two terms are the contributions from the zero-point and vibrational (entropy) energies, respectively. The summations run over all phonon wave vectors and phonon modes in the first Brillouin zone (BZ).

The temperature dependence entering the last term in Eq. (1) was evaluated in the harmonic approximation at constant volume. Technically, this is an approximation, since high temperatures would cause the volume of the structure to expand. The next order correction would include the volume dependence of the phonon frequencies in the quasiharmonic approximation [57]. Furthermore, even the quasiharmonic approximation may break down at very high temperatures. When atoms are significantly displaced from their equilibrium positions upon heating, anharmonic effects may become important, as recently demonstrated for black phosphorus [58]. In practice, the $F(P, T)$ term of G was calculated from 0 to 1600 K in a postprocessing step using PHONOPY [53] with a $10 \times 10 \times 10$ q-point mesh.

Raman intensities were calculated in frozen-phonon approximation together with the frequency-dependent dielectric tensor [59–61]. The many-body electron-electron effects were included through the GW correction [62] to the electronic structure and thus the dielectric response [61]. Single-shot G_0W_0 calculations were performed with a reduced k-point grid sampling of $5 \times 5 \times 5$ for computational feasibility. The dielectric function was found to be well converged with respect to the k-point sampling even with the reduced sampling. A total of 192 (3× the default setting) bands were included in the GW step together with a response-function cutoff of 80 eV and NOMEGA = 36. The GW band-gap convergence was carefully tested with respect to these settings and was found to be within 0.1 eV. Additional procedural details and a theoretical background of Raman intensity calculations are provided in the SM [50].

III. RESULTS AND DISCUSSION

At ambient conditions bulk ReS_2 crystallizes in a low-symmetry triclinic structure [space group $P-1$ (no. 2), point group $C_i(-1)$]. This phase is known as the distorted $1T$ structure. The distortion observed in ReS_2 is due to a Peierls distortion induced by the extra valence electron in the group-VII Re atoms compared to W atoms [40]. The unit cell of bulk ReS_2 contains a single layer comprised of two formula units. Under the effect of pressure, ReS_2 undergoes a phase transition to a structure with a somewhat different stacking configuration and thus a different unit-cell shape [23,33,34]. This high-pressure structure also consists of two formula units and belongs to the same space group as the ambient one. Different naming conventions for these two structures can be found in the literature. Here, the convention of Wang *et al.* is adopted according to which the ambient structure is denoted as distorted $1T$ and the high-pressure phase as distorted $1T'$ structure [34]. For brevity, however, the two structures will be referred to as $1T$ and $1T'$ throughout this work.

Calculated structural parameters of the distorted $1T$ phase are in good agreement with experimental and previously reported DFT results (see the SM [50]). The lattice parameters of the distorted $1T'$ structure have not been measured directly to date. However, the calculated lattice parameters in this work reproduce those previously reported using DFT [33,34]. Both structures were found to be dynamically stable over the complete pressure range studied here, as indicated by the absence of imaginary phonon modes in their phonon band structures (see details in the SM [50]). This shows that both structures correspond to a deep enough local minimum of the potential landscape.

A. Thermodynamics

The structural phase transition from $1T$ to $1T'$ has been shown to occur experimentally between 7 and 11 GPa [23,33,34,36]. First-principles calculations predicted the phase transition to take place between 0.1 and 3 GPa, depending on which DFT functional was used [33,34]. The predictions were based on evaluating the enthalpy difference between the two structures. This work established that the PBE + vdW functional is required to correctly reproduce the experimental bulk modulus of ReS_2 and to study the structural changes under pressure. Thus, the pressure-induced phase transition will be examined using this functional. Moreover, since the aforementioned experiments were conducted at room temperature, the effects of temperature on the energy differences between the $1T$ and $1T'$ phases have been included as well. This is achieved by considering the Gibbs free

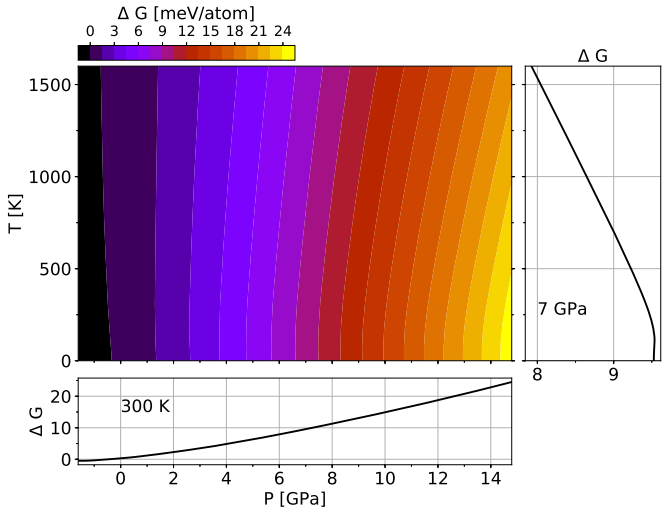

FIG. 1. Calculated Gibbs free-energy difference $\Delta G = G^{1T} - G^{1T'}$ between the $1T$ and $1T'$ phases as a function of hydrostatic pressure and temperature (main contour plot). Cuts through the two-dimensional plot at constant pressure (right side plot) and at constant temperature (bottom plot) are provided. Negative pressure corresponds to uniform strain on the structures. As a result of the self-consistent pressure calibration (see Sec. II), the exact DFT pressures are slightly different for the two phases. The $G(P, T = \text{const})$ points for each phase were first interpolated on a uniform grid of test pressures with 101 points and the difference ΔG was then evaluated.

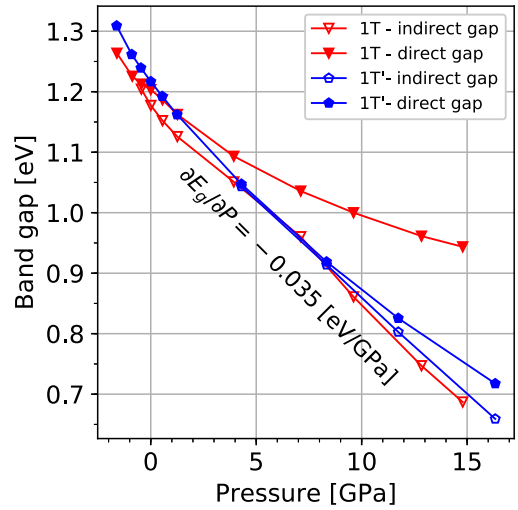

FIG. 2. Calculated electronic band gap of bulk ReS_2 in the distorted $1T$ and distorted $1T'$ phases as a function of pressure. Open markers indicate an indirect gap and filled markers a direct gap, respectively. The whole 3D-BZ with dense k-space grids was considered for band-gap evaluation. The energy difference between the valence-band maximum (VBM) and conduction-band minimum (CBM) was fitted using linear regression. The average slope $\partial E_g/\partial P$ is indicated along the curves and is essentially identical for $1T$ and $1T'$.

energy $[G(P, T) = F(P, T) + PV]$ instead of the enthalpy $[H(P) = E_{gs}(P) + PV]$. The two potentials are identical at $T = 0$ except for the zero-point energy contribution to the free energy term in G [Eq. (1)]. Note that the zero-point energy was found to be essentially identical for $1T$ and $1T'$. Figure 1 shows the difference in Gibbs free energy between the $1T$ and $1T'$ phases of bulk ReS_2 as a function of pressure and temperature. For all pressures $P \geqslant 0$ the energy difference is larger than zero indicating that the $1T'$ phase is energetically more favorable than $1T$ regardless of temperature. This seems to contradict the experimental observation that ReS_2 is typically found in the distorted $1T$ phase under ambient conditions. This issue will be discussed in more detail below.

For very small pressures $\Delta G \approx 0$, the two structures are found to be energetically degenerate. The $1T$ and $1T'$ phases differ predominantly by their layer-stacking order. Thus, the finding of $\Delta G \approx 0$ might be in alignment with the previously reported energetics of different stackings in bilayer ReS_2. Namely, it has been shown that deviations from the *AA* stacking in the bilayer system are energetically very similar [22]. At constant pressure, however, ΔG decreases somewhat with increasing T resulting in a smaller energy gain for the $1T'$ structure compared to $1T$ at high temperatures; see right plot in Fig. 1. Furthermore, for small uniform strains of about -1.5 GPa (equivalent to $\sim 8\%$ volume strain), the $1T$ phase becomes energetically slightly more favorable than the $1T'$ phase with small $\Delta G < 0$. Naturally, these findings have to be viewed in the context of statistical distributions. The structure with the smaller Gibbs free energy has a higher probability of forming at given conditions, while the other one can be formed as well, only with lower probability. Nevertheless, these findings for $P < 0$ and high T might provide an explanation for why the $1T$ phase is typically observed experimentally at ambient conditions.

ReS_2 is commonly synthesized by chemical vapor deposition (CVD). The CVD method is based on powder vaporization, where solid precursors of Re and S are treated under high temperatures until they vaporize and then are brought to react and form a crystal on a substrate [63]. The high-temperature annealing conditions during ReS_2 growth might be more favorable for the formation of the distorted $1T$ phase. Furthermore, the CVD substrate might exert local strains during ReS_2 crystal formation. These strains could reach relatively large values locally. Following the general trend for decreasing $\Delta G < 0$ with increasing strain in Fig. 1, large local strains might further make the $1T$ structure more energetically favorable.

While Fig. 1 provides a rationale for the stability of the $1T$ phase during typical growth procedures, it does not provide an answer to the question at which exact (P, T) conditions the transition to the $1T'$ phase occurs. However, if we estimate the required energy gain for the $1T'$ structure to form to be at least a few tens of meV/atom, then at room temperature the phase transition would occur between 7 and 8 GPa. This is in good agreement with the experimentally reported value of about 8 GPa [23,34].

B. Electronic properties

Figure 2 shows the calculated electronic band gap of the two phases of bulk ReS_2 as a function of pressure. We note that different functionals and the *GW* correction were tested for band-gap evaluation for the $1T$ phase all giving similar results; see the SM [50]. In the distorted $1T$ phase, the band

gap is direct for small negative pressures and becomes indirect at $P = 0$ GPa. The indirect band gap decreases in good approximation linearly with increasing P with a pressure coefficient of $\partial E_g/\partial P = 35$ meV/GPa. The direct gap decreases as well, but at a smaller rate and deviating from a linear trend. However, the difference between the indirect and direct gaps is relatively small, < 0.1 eV for $P < 9$ GPa. Thus, it is not possible to tell with confidence whether the band gap of $1T$ bulk ReS_2 would manifest as a direct or indirect one in a given practical setting. However, as the difference between the indirect and direct gaps further increases for $P \geqslant 9$ GPa, an indirect band-gap character can be expected in that pressure range. In contrast, for the distorted $1T'$ phase, the direct and indirect band gaps are essentially degenerate in the entire pressure range. Note that the linear pressure coefficient is practically the same as for the $1T$ phase, while the band-gap type (direct vs indirect) is different. Moreover, the band gaps of $1T$ and $1T'$ are very similar, with a difference of less than 0.05 eV for all pressures.

The negative pressure coefficient has been previously rationalized from orbital analysis [35]. The p_z orbitals on the sulfur atoms, that enclose ReS_2's van der Waals gap from above and below, have a significant out-of-plane amplitude that extends into the gap. As pressure rises, the vdW gap shrinks, increasing the overlap between p_z orbitals. This results in an increase in energy of the p_z-like states due to increased antibonding interactions between opposing p_z lobes [35,64]. The interlayer distance decreases more rapidly with increasing pressure in the $1T'$ phase. Thus, the Coulomb repulsion between overlapping p_z orbitals has a larger effect in $1T'$. This accounts for the stronger decrease of the direct gap with pressure in the $1T'$ phase compared to that in $1T$. In addition, the different stacking order in $1T'$ seems to be responsible for the band gap to remain direct and nearly direct, while a transition from the nearly direct to indirect gap takes place in $1T$.

These findings indicate a pathway for ReS_2 to be used as a robust nearly direct gap material via pressure-induced $1T$ to $1T'$ phase transition. However, in order to exploit the structural phase transition under pressure, exact knowledge of the structural phase is required. Such knowledge can be obtained through characterization using vibrational spectroscopy methods as will be shown next.

C. Vibrational properties: High-frequency intralayer modes

Both the ambient and high-pressure phases of ReS_2 have a unit cell with 12 atoms and thus support 36 vibrational modes. At the Γ point only two symmetry types of phonon modes are allowed in the low-symmetry point group C_i of ReS_2. Of the 36 vibrational modes, 18 modes belong to the irreducible representation A_u, three of which are translational (acoustic) modes. The remaining 15 optical A_u modes are infrared (IR) active. The other 18 A_g modes are Raman active. All optical modes are nondegenerate in ReS_2 in contrast to doubly degenerate in-plane vibrations in 2H MX_2 TMDs. The 18 Raman-active phonon modes of ambient bulk ReS_2 have been characterized with respect to their frequencies, symmetry, and atomic vibrations previously [38–40,63]. Our DFT results are in good agreement with the literature. Since all the Raman- (IR-) active modes have the same symmetry, the modes were simply numbered in order of increasing vibrational frequency throughout this work. The evolution of the Raman-active modes under the effect of pressure has been discussed before using experimental Raman spectroscopy [23,34]. In contrast, IR-active modes have not received much attention thus far. Furthermore, the vibrational properties of the high-pressure distorted $1T'$ structure and their pressure dependence have not been studied theoretically. Here, we provide detailed discussions on the differences and similarities of the vibrational properties of the two ReS_2 phases and suggest pathways for practical phase discrimination using vibrational spectroscopy methods.

Phonon frequencies of all Raman- and IR-active modes as a function of pressure in the two phases are shown in Fig. S7 of the SM [50]. All mode frequencies increase (blueshift) monotonically with increasing pressure. Such a frequency blueshift is typically due to an effective stiffening of the force constants arising from bond shortening under pressure. However, in certain modes in which the atomic bond lengths do not change significantly during the vibrations, application of pressure can induce a global force constant softening and lead to a redshift of that phonon mode [65]. Such counterintuitive behavior is not observed for bulk ReS_2. Thus, all vibrational modes can be generally expected to be characterized by significant changes of atomic bond lengths.

As a first-order approximation the $\omega(P)$ curves were fitted to linear functions to allow for a quantitative comparison between the modes. The resulting $\partial\omega/\partial P$ slopes of the Raman-active modes are collected in Table I. Experimental ω vs P data are available for some of the Raman-active modes as well. However, experimentally a phase transition from $1T$ to $1T'$ is reported around 8 GPa [23,34]. Thus, the experimental $\omega(P)$ points below and above the transition pressure should be attributed to the $1T$ and $1T'$ phases, respectively. Using the *WebPlotDigitizer* tool [66], $\omega(P)$ points were extracted from Figs. 2(d)–2(e) of Ref. [23] and from Fig. 3(b) of Ref. [34]. In this way, three to five data points each below 8 GPa and between 8 and 15 GPa were collected and then fitted to linear functions. The calculated phonon frequencies were fitted over the same pressure range as the experimental ones for each phase. Five data points up to 8 GPa and three data points above 8 GPa were used for the $1T$ and $1T'$ phases, respectively. The calculated frequencies for each phase are available in the complete pressure range, but since they do not present a perfectly linear evolution with pressure, a fit over the complete pressure range would make the comparison with experiment inconsistent.

In Table I, more than half of the calculated $\partial\omega/\partial P$ slopes, for which the experimental values are available, agree with their experimental counterparts within their respective error bars. We note a number of differences between the two experiments previously reported in the literature. This might be due to difficulties in experimental mode assignment. Specifically, all the reported modes of Yan *et al.* [23] at $P = 0$ are 3–5 cm^{-1} lower than typically reported [38–40]. For example, the Raman mode no. 1 ($A_{1g} - 1$ in Ref. [23]) is found at 131 cm^{-1} while it was previously reported at 140 cm^{-1} [38]. The mode at 131 cm^{-1} in Ref. [23] could actually be a disorder-activated IR mode with frequency close to a Raman-active one

TABLE I. Calculated phonon frequencies of Raman-active modes at 0 and 8 GPa for $1T$ and $1T'$ phases, respectively, together with their $\partial\omega/\partial P$ slopes obtained by linear regressions to the calculated $\omega(P)$ data points in Fig. S7. Available experimental values are indicated for comparison. The slope uncertainty is the linear-fit standard error. Details on the fitting procedure are provided in the main text.

	Distorted $1T$				Distorted $1T'$			
Mode no.	ω_0 (cm^{-1})	$\partial\omega/\partial P$ (cm^{-1}/GPa)	Expt. [23]	Expt. [34]	ω_8 (cm^{-1})	$\partial\omega/\partial P$ (cm^{-1}/GPa)	Expt. [23]	Expt. [34]
1	133.5	1.13(5)	0.23(3)		135.3	0.77(2)	0.09(5)	
2	139.2	0.96(3)	1.46(7)		143.2	0.80(2)	0.80(17)	
3	145.7	0.80(1)	1.32(11)	0.59(8)	149.1	0.49(1)	0.41(12)	0.44(29)
4	156.8	0.45(1)	0.79(5)	0.38(9)	161.1	0.50(2)	0.54(11)	0.46(39)
5	205.2	1.09(2)	1.48(13)	1.02(9)	215.3	0.86(2)	0.55(20)	0.86(26)
6	225.0	1.14(3)	1.14(13)	0.89(8)	234.8	0.82(2)	0.55(6)	0.67(32)
7	261.4	1.60(7)			274.4	1.28(2)		
8	267.2	2.05(3)			288.8	1.90(6)		
9	293.1	1.61(3)	1.25(13)		308.4	1.71(2)	0.97(3)	
10	294.8	1.66(3)	1.49(16)		310.3	1.58(2)	0.93(4)	
11	302.3	1.94(3)			319.6	1.97(4)		
12	307.8	1.88(2)			330.5	1.90(7)		
13	332.6	2.55(5)		2.39(19)	359.2	2.64(2)		2.74(22)
14	353.4	2.12(4)			384.7	2.11(7)		
15	364.7	2.87(5)			387.5	2.48(9)		
16	391.2	2.37(4)			414.9	2.21(1)		
17	402.8	2.28(3)	3.03(15)		428.5	2.29(4)	2.30(5)	
18	421.6	3.02(6)	3.51(24)	3.34(13)	448.3	2.78(7)	2.72(11)	3.60(33)

[40]. Indeed, looking ahead to the analysis of the calculated IR-active modes, the IR mode no. 1 is found around 130 cm^{-1}. Its $\partial\omega/\partial P$ slope of 0.3 cm^{-1}/GPa is in agreement with the experimental one of the alleged Raman mode no. 1 of 0.23 cm^{-1}/GPa (see Tables I and II).

The Raman mode no. 18 blueshifts most strongly under the effect of pressure in both phases. This mode is characterized by the out-of-plane motion of the S atoms with slight movements of the Re atoms (animations of the discussed modes can be viewed in the SM [50]). As the out-of-plane lattice parameters decrease most strongly with increasing pressure (see Fig. S2 [50]), the large $\partial\omega/\partial P$ slope of this mode reflects the corresponding change of the out-of-plane force constants with pressure. In addition, the two phases differ primarily by their layer stacking and interlayer distance; see Figs. S1 and S3 in the SM [50]. These out-of-plane characteristics are probed by the vibration of mode no. 18. Thus, intuitively this mode should also exhibit the largest slope difference for $1T$ and $1T'$. However, contrary to expectations, the slopes of this mode are quite similar in the two phases. Apparently, the global force constant differences for a given vibration can lead to quite similar $\partial\omega/\partial P$ slopes, making the discrimination between the two phases based on Raman shifts particularly challenging.

TABLE II. Similar to Table I, but for IR-active modes.

	Distorted $1T$		Distorted $1T'$	
Mode no.	IR ω_0	$\partial\omega/\partial P$	IR ω_8	$\partial\omega/\partial P$
1	133.2	0.30(1)	150.7	1.15(4)
2	153.3	0.68(2)	162.8	0.91(2)
3	213.1	1.39(3)	220.6	0.81(2)
4	260.6	2.45(12)	273.1	1.51(4)
5	266.0	3.10(7)	277.1	1.68(1)
6	277.0	2.64(6)	298.3	2.09(6)
7	294.8	1.60(2)	316.2	1.55(5)
8	296.2	2.35(4)	319.5	2.23(6)
9	307.6	1.79(2)	325.5	2.28(4)
10	330.0	2.17(2)	355.2	2.15(7)
11	351.3	2.70(5)	366.9	1.90(2)
12	362.0	2.34(3)	385.6	2.27(5)
13	381.7	2.31(4)	412.8	2.57(7)
14	406.9	2.03(3)	437.0	2.20(8)
15	437.5	2.30(2)	456.7	2.22(2)

Given the agreement between the calculated and experimental $\partial\omega/\partial P$ trends, analogous slopes of IR-active modes were predicted next and are summarized in Table II. Raman and IR modes evolve with similar sensitivity to pressure. However, the difference in the $\partial\omega/\partial P$ response for a given mode between the ambient and high-pressure phases is larger for IR modes than for Raman-active modes.

Figure 3 shows the Raman- and IR-active modes with the largest absolute slope difference between the ambient and high-pressure phases. Inspection of atomic displacements in these vibrations allows for rationalization of the different ω vs. P behavior between $1T$ and $1T'$. In the Raman-active mode no. 15, the S atoms are mainly displaced within the plane of each layer in a similar fashion for $1T$ and $1T'$. The out-of-plane displacements of the Re atoms are slightly larger in $1T'$ than in $1T$, but overall the vibrations are very similar. This explains the relatively close $\partial\omega/\partial P$ slopes in the two phases. In contrast, the IR-active mode no. 5 presents clear differences in the corresponding atomic displacements in $1T$ and $1T'$. In both phases, this mode features relatively large movements of the sulfur atoms in the out-of-plane direction. However, the vibration in $1T$ is accompanied by sizable changes of the

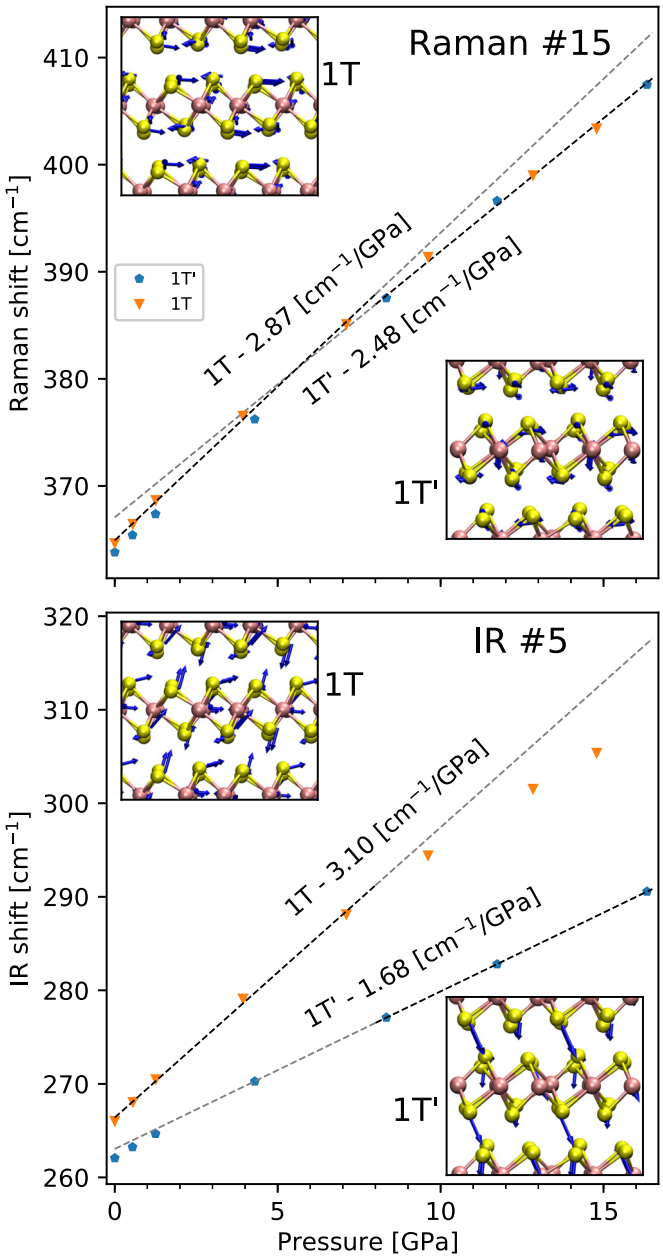

FIG. 3. Comparison of calculated phonon frequencies as a function of pressure for the $1T$ and $1T'$ phases. Dashed lines indicate linear fit functions and fit results for the slopes are given along the lines. The details on the linear fit procedures are discussed in the text. The figure insets provide visualizations of the atomic vibrations in the corresponding mode. Top panel: The Raman-active mode no. 15 that has the largest absolute difference between the $\partial\omega/\partial P$ for the $1T$ and $1T'$ phases. Bottom panel: Like top panel, but for the IR-active mode no. 5.

intralayer Re-Re bonds. In $1T'$, on the other hand, the Re atoms move only slightly and in phase with each other, leaving the intralayer Re-Re bonds practically unchanged. Similarly, IR-active modes nos. 1, 4, and 11 also feature significant changes of the interlayer distances during their vibrations, but also distinct atomic movements within a single layer in $1T$ and $1T'$. The overall differences in structural and vibrational characteristics in the $1T$ and $1T'$ phases account for the distinct $\partial\omega/\partial P$ slopes of the IR modes and can be exploited for phase-transition detection.

The analysis presented here highlights another important issue. Namely, the experimental mode assignment and mode tracking with pressure can be impeded by the fact that a given mode of $1T'$ can be close in frequency to a different one in $1T$. For example, results shown in Fig. S7 suggest a sizable discontinuity in mode frequency when going from $1T$ to $1T'$ for Raman-active modes nos. 1, 2, 3, 14, and 17. But the experimental $\omega(P)$ curves of modes no. 3 ($A_{1g}-1$) and no. 17 ($A_{1g}-3$) of Yan *et al.* [23] are relatively smooth at the alleged transition pressure. Thus, the information on the ω vs P evolution presented here should allow for the unambiguous tracking of the phase transition between the $1T$ and $1T'$ phases.

D. Vibrational properties: Low-frequency interlayer modes

Low-frequency (LF) interlayer modes correspond to quasi-rigid movements of atomic layers as individual units. Rigid in-plane vibrations of layers parallel to each other are called shear modes (S modes) and out-of-plane vibrations are referred to as layer breathing modes (LB modes) [37,67]. These layer modes can be extremely useful for studying weak interlayer interactions in layered materials [37,67]. Finding a way to quantify the interlayer interactions in bulk ReS_2 is particularly intriguing, since this material has been shown to behave almost like decoupled monolayers [13].

Bulk ReS_2 consists of a single layer in its unit cell and it follows that low-frequency interlayer modes are not Raman active in the bulk. For the primitive unit cell, the interlayer shear and breathing modes are located at the Z [0,0,0.5] and L [0.5, 0.5, 0] point in the first BZ of the $1T$ and $1T'$ structures, respectively. Note that the Z and L points are along the out-of-plane direction of the corresponding structure. Since they are at a non-Γ point in the bulk, they cannot be directly probed by first-order Raman spectroscopy. However, they can be studied by inelastic neutron scattering and inelastic x-ray scattering. The interlayer vibrational modes and phonon dispersion relations have been probed by inelastic neutron and/or x-ray scattering for many layered materials, such as graphite, hexagonal boron nitride, MoS_2, and black phosphorus [68–74]. However, to the best of our knowledge, neither of the aforementioned experimental techniques have been used in bulk ReS_2 for phonon dispersion analysis. Such analysis might prove useful especially in the context of the application of pressure for phase discrimination.

The interlayer mode frequencies are extremely sensitive to the stacking order in layered materials and they can be directly linked to interlayer coupling strengths through the use of the linear chain model (LCM) [37,67]. In the LCM each layer is modeled is a single ball with mass density μ (in units of mass per unit area) and the layers arrange as a chain of harmonic oscillators. The frequencies in of the bulk are given by [37]

$$\omega(S_{\text{bulk}}) = (1/\pi c)\sqrt{K^{\parallel}/\mu}, \tag{2}$$

$$\omega(\text{LB}_{\text{bulk}}) = (1/\pi c)\sqrt{K^{\perp}/\mu}, \tag{3}$$

where $K^{\parallel}$ ($K^{\perp}$) is the in-plane (out-of-plane) interlayer force constant per unit area, μ is the total mass per unit area of

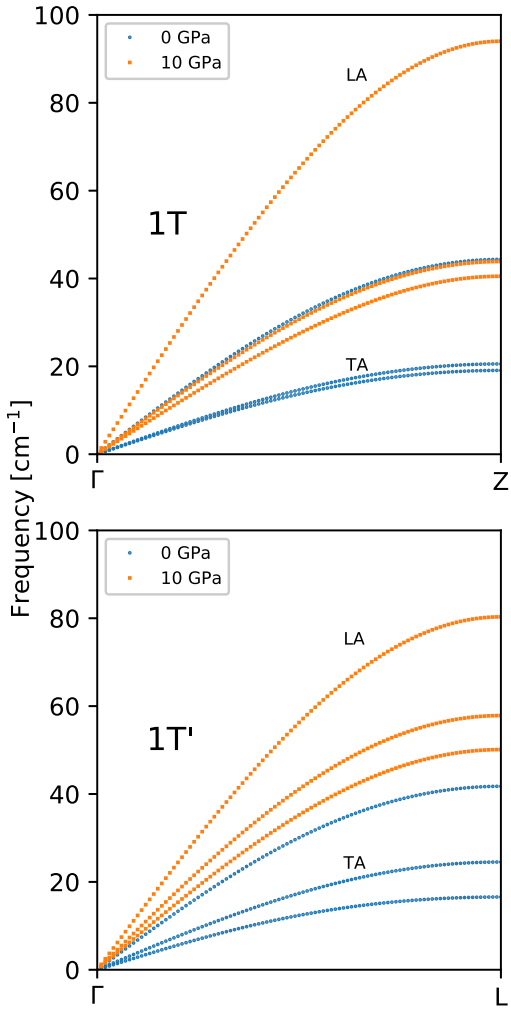

FIG. 4. Calculated phonon dispersion relations of the acoustic modes in $1T$ (top panel) and $1T'$ (bottom panel) along the out-of-plane direction. Two representative pressures are compared for each structure. These modes correspond to layer shearing (TA) and layer breathing (LA) modes off Γ point as discussed in the text. Their frequencies at the zone boundary Z ($1T$) or L ($1T'$) are summarized in Table III.

each layer, and c is the speed of light. The interlayer force constants have been determined from the above expression with the knowledge of $\omega(S_{\text{bulk}})$ and $\omega(\text{LB}_{\text{bulk}})$ (from experiment or DFT) for many layered materials [37]. In this work, the corresponding results are reported for the $1T'$ phase of bulk ReS_2, and the effect of pressure on the interlayer force constants of both $1T$ and $1T'$ phases is explored.

Figure 4 shows the dispersion relations of acoustic phonons in $1T$ and $1T'$ ReS_2. The path in q space is along the out-of-plane direction, which corresponds to $\Gamma \rightarrow Z$ and $\Gamma \rightarrow L$ for $1T$ and $1T'$, respectively. Full dispersion relations in the complete BZ can be found in the SM [50,75]. For each phase, the dispersions at two pressures are compared. Overall, for both phases a typical hardening of all branches under the effect of pressure is observed [74]. Note that just as in anisotropic black phosphorus, the in-plane anisotropy of ReS_2 causes the S modes to split. This splitting is much larger in the $1T'$ phase than in $1T$. Furthermore, the LB mode in both phases is significantly more sensitive to pressure than the S modes. This is expected, as the LB mode probes $K^{\perp}$, which changes the most under pressure.

TABLE III. Calculated frequencies of LF interlayer modes obtained at the Z and L points of the first BZ for $1T$ and $1T'$ phase, respectively. Interlayer force constants $K^{||}$ and $K^{\perp}$ were calculated using the linear chain model for the LF modes. Unlike in traditional hexagonal TMDs, the two S modes are not degenerate due to the in-plane anisotropy [37].

P (GPa)	Phase	$\omega(S)$ (cm^{-1})	ω(LB) (cm^{-1})	$K^{\|\|}$ (10^{19} N/m^3)	$K^{\perp}$ (10^{19} N/m^3)
0	$1T$	19.08/20.55	44.35	1.49/1.72	8.03
	$1T'$	16.56/24.52	41.75	1.12/2.45	7.12
10	$1T$	40.51/43.87	94.01	6.79/7.86	36.08
	$1T'$	50.11/57.85	80.32	10.25/13.66	26.34

The interlayer mode frequencies at the high-symmetry non-Γ points are summarized in Table III. The split of the S modes is relatively small in $1T$ and increases only slightly under pressure, from a difference of about 1–3 cm^{-1}. In contrast, in $1T'$ the S modes are split by about eight wave numbers and this split remains the same under pressure. For both phases, pressure has the effect of hardening all the LF modes by a factor of 2–3. Interestingly, at high pressure the S modes are harder in $1T'$ than in $1T$, while the reverse is true for the LB mode. This result can be linked to the bond angle between S atoms that enclose the vdW gap. In $1T$ this glide angle remains practically constant with pressure; see the SM [50]. Thus, the LB mode hardening at $P = 10$ GPa is almost exclusively due to reduced interlayer distance. In $1T'$, however, both the interlayer separation and the glide angle decrease with pressure. The former factor dominates and leads to the observed mode hardening compared to $P = 0$. The latter mechanism is found to counteract and compensate the hardening rate.

The interlayer force constants $K^{\|}$ and $K^{\perp}$ determined from the extracted LF mode frequencies using Eq. (2) are also given in Table III. The values for ambient $1T$ ReS_2 are in agreement with previous results [37,76]. In the case of the $1T'$ structure at 0 GPa, the force constants are quite similar to $1T$, even though slightly smaller for S and LB modes. However, at 10 GPa, $K^{\|}$ reaches values typical of its $K^{\perp}$ counterpart at ambient conditions in most layered materials [37]. Moreover, the $K^{\perp}$ constants increase dramatically. Thus, these results provide a quantitative confirmation to the intuition of pressure increasing the interlayer couplings.

The phonon dispersion analysis presented here could be useful for a clear phase discrimination between the ambient and high-pressure phases of bulk ReS_2. This is possible because the LF modes are extremely sensitive to stacking order and interlayer distance, much more so than the high-frequency intralayer modes. In addition, such analysis within the LCM provides quantitative insights into interlayer couplings in decoupled bulk ReS_2. Thus, experimental corroboration of these results is very desirable, especially since studying bulk samples under pressure is feasible for inelastic neutron/x-ray scattering.

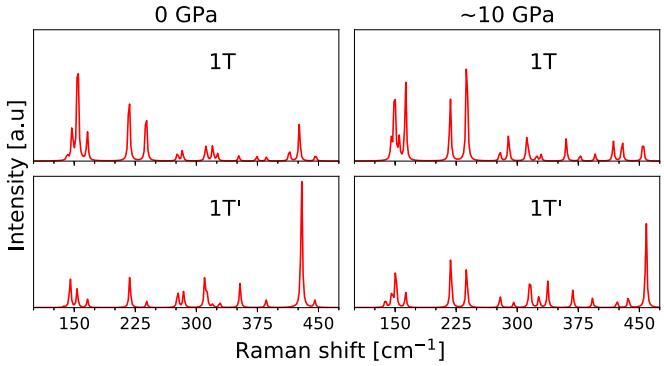

FIG. 5. Calculated polarization-angle averaged Raman spectra of $1T$ and $1T'$ bulk ReS_2 at ambient (0 GPa) and high (∼10 GPa) pressure for back-scattering setup parallel to the out-of-plane axis. The frequency-dependent dielectric tensor $\varepsilon(\omega)$ was evaluated at $\omega = 2.83$ eV. This is to account for the difference in calculated and experimental band gap, i.e., to keep the experimental $E_{\text{gap}}/E_{\text{laser}}$ ratio constant. A typical red Raman laser with 633 nm wavelength (1.96 eV) was assumed. Calculation settings are detailed in SM [50].

E. Raman spectra

We established that the frequencies of the Raman-active modes are not very sensitive to the phase of ReS_2. In contrast, Raman intensities might show more significant variations upon structural phase transition from $1T$ to $1T'$. The appeal of using Raman spectroscopy lies in its practical simplicity compared to experimental IR spectroscopy and neutron/x-ray scattering measurements. However, from the viewpoint of first-principles calculations, accurate prediction of Raman intensities is challenging. Here, the frozen-phonon expression for the Raman susceptibility was used together with the frequency-dependent dielectric tensor in order to capture resonance effects [61]. However, in our current work, while many-body electron-electron effects were included through the *GW* correction to the electronic structure and thus the dielectric response, excitonic effects (i.e., electron-hole interactions) have been neglected due to computational limitations.

Figure 5 shows the calculated Raman spectra averaged over the polarization angle of a red excitation laser (633 nm) in a back-scattering setup along the out-of-plane direction. First, the spectrum of ambient $1T$–ReS_2 is in good qualitative agreement with the corresponding experimental one [38]. The most intense band is associated with mode no. 3 followed by the one corresponding to mode no. 5. However, the next most intense bands are linked to modes no. 6 and no. 2, while experimentally the third most intense band belongs to mode no. 4 followed by mode no. 6. Quantitative agreement is not expected at this stage, as will be discussed later.

At zero pressure, the most intense band in the spectrum of $1T'$–ReS_2 belongs to mode no. 17. The modes below 250 cm^{-1} have much lower intensity, particularly in contrast to more intense bands of $1T$ in that range. This finding emphasizes that while the structural and vibrational features of the two phases are very similar (under these simulated conditions), their Raman response can be dramatically distinct. Under pressure the relations between peaks change in both $1T$ and $1T'$. In $1T$, the most intense bands are now those of modes no. 6 and no. 4, followed by almost equal intensities of bands no. 2 and no. 5, while the intensity of mode no. 3 has diminished significantly. In $1T'$, Raman mode no. 18 is now the most intense band. However, in experiment one would only have access to the spectrum of $1T$ at 0 GPa and that of $1T'$ at 10 GPa out of the four shown in Fig. 5, because of the phase transition. Interestingly, the relative intensities of the first six bands in the spectrum of $1T'$ at 10 GPa are similar to their ambient $1T$ counterparts, thus making a differentiation between the two phases difficult. Note that the high intensity of the 18th band in high-pressure $1T'$ is the most prominent feature compared to ambient $1T$ and could be helpful for phase discrimination.

The above findings should be considered with caution. Experimentally ReS_2 is known to exhibit an intricate resonant Raman behavior [40]. The polarization-averaged spectrum of the ambient $1T$ structure for a red excitation laser shown above seems to agree well with experiment. However, analogous spectra for other laser wavelengths and for individual polarization angle values could not be reproduced fully. First, many-body excitonic effects are neglected in our calculations owing to the prohibitive computational cost. Second, the experimental polarization setup cannot be modeled exactly in calculations, while the polarization of the incident and scattered light could strongly affect Raman intensities. In addition, the application of pressure can further complicate the situation. As the band gap decreases with pressure, the resonant Raman response can change as well. Given the negative pressure coefficient, the decreasing band gap might also have an effect on the excitonic details. Nevertheless, our calculations do suggest that Raman intensities of ReS_2 are sensitive to both phase and pressure.

All in all, these findings emphasize the importance of method development for resonant Raman calculations. Recently, an efficient perturbative approach that reduces the number of required *GW* and BSE (Beth-Salpeter equation) calculations has been suggested [77]. In future work this method should be considered especially for low-symmetry and anisotropic materials such as ReS_2.

IV. CONCLUSION

In this work, we have systematically studied the thermodynamic, electronic, and especially vibrational properties of two phases of bulk ReS_2 under the effect of pressure. The ambient distorted $1T$ and the high-pressure distorted $1T'$ structures differ mainly by their layer-stacking order. For small pressures, they are energetically degenerate. This suggests that there is no stacking preference at ambient conditions. However, under high temperature the degeneracy is lifted slightly in favor of the $1T$ structure. Applied pressure leads to the $1T'$ phase being clearly energetically more favorable.

Differences in electronic properties of the two phases can potentially be useful for practical applications. The ambient distorted $1T$ phase exhibits a nearly direct to indirect gap transition at elevated pressure. However, the distorted $1T'$ phase remains a nearly direct gap material under increasing pressure. Control over the $1T$ to $1T'$ phase transition could allow for ReS_2 to be used as a robust (nearly) direct gap material.

As a means of characterization, vibrational properties as a function of pressure in the two phases have been discussed in detail. Optical modes exhibit a change of slope in their fairly linear $\omega(P)$ curves between the $1T$ and $1T'$ structures. However, the change in slope is more pronounced for IR-active than for Raman-active modes. Thus, the former seem to be more suitable for phase-transition detection. In addition, acoustic modes away from the Γ point (i.e., the interlayer vibrational modes) are even more sensitive to differences in stacking and interlayer distance between $1T$ and $1T'$ than the optical ones. These interlayer modes can be accessed experimentally by inelastic neutron and x-ray scattering to reveal the phase transition and pressure effect.

ACKNOWLEDGMENTS

N.S. was supported by National Science Foundation Grant No. EFRI 2-DARE (EFRI-1542707). A.Y. was supported by the National Science Foundation (Award No. 1608171). J.G. was supported by the NY State Empire State Development's Division of Science, Technology and Innovation (NYSTAR) through Focus Center-NY-RPI Contract No. C150117. A portion of this research used resources at the Center for Nanophase Materials Sciences, which is a U.S. Department of Energy Office of Science User Facility. Supercomputing resources used for this work were provided by the Center for Computational Innovations at RPI. Useful discussions with Prof. H. Terrones and B. Van Troeye are gratefully acknowledged.

[1] Q. H. Wang, K. Kalantar-Zadeh, A. Kis, J. N. Coleman, and M. S. Strano, Nat. Nanotechnol. **7**, 699 (2012).
[2] S. Z. Butler, S. M. Hollen, L. Cao, Y. Cui, J. A. Gupta, H. R. Gutiérrez, T. F. Heinz, S. S. Hong, J. Huang, A. F. Ismach, E. Johnston-Halperin, M. Kuno, V. V. Plashnitsa, R. D. Robinson, R. S. Ruoff, S. Salahuddin, J. Shan, L. Shi, M. G. Spencer, M. Terrones *et al.*, ACS Nano **7**, 2898 (2013).
[3] H. Schmidt, F. Giustiniano, and G. Eda, Chem. Soc. Rev. **44**, 7715 (2015).
[4] H. Wang, H. Yuan, S. Sae Hong, Y. Li, and Y. Cui, Chem. Soc. Rev. **44**, 2664 (2015).
[5] S.-L. Li, K. Tsukagoshi, E. Orgiu, and P. Samori, Chem. Soc. Rev. **45**, 118 (2016).
[6] D. Akinwande, C. J. Brennan, J. S. Bunch, P. Egberts, J. R. Felts, H. Gao, R. Huang, J.-S. Kim, T. Li, Y. Li, K. M. Liechti, N. Lu, H. S. Park, E. J. Reed, P. Wang, B. I. Yakobson, T. Zhang, Y.-W. Zhang, Y. Zhou, and Y. Zhu, Extreme Mech. Lett. **13**, 42 (2017).
[7] W. Choi, N. Choudhary, G. H. Han, J. Park, D. Akinwande, and Y. H. Lee, Mater. Today **20**, 116 (2017).
[8] Q. Li, J. Lu, P. Gupta, and M. Qiu, Adv. Opt. Mater. **7**, 1900595 (2019).
[9] D. W. Shen, B. P. Xie, J. F. Zhao, L. X. Yang, L. Fang, J. Shi, R. H. He, D. H. Lu, H. H. Wen, and D. L. Feng, Phys. Rev. Lett. **99**, 216404 (2007).
[10] M. Calandra and F. Mauri, Phys. Rev. Lett. **106**, 196406 (2011).
[11] U. Chatterjee, J. Zhao, M. Iavarone, R. Di Capua, J. P. Castellan, G. Karapetrov, C. D. Malliakas, M. G. Kanatzidis, H. Claus, J. P. C. Ruff, F. Weber, J. van Wezel, J. C. Campuzano, R. Osborn, M. Randeria, N. Trivedi, M. R. Norman, and S. Rosenkranz, Nat. Commun. **6**, 6313 (2015).
[12] H. Suderow, V. G. Tissen, J. P. Brison, J. L. Martínez, and S. Vieira, Phys. Rev. Lett. **95**, 117006 (2005).
[13] S. Tongay, H. Sahin, C. Ko, A. Luce, W. Fan, K. Liu, J. Zhou, Y.-s. Huang, C.-h. Ho, J. Yan, D. F. Ogletree, S. Aloni, J. Ji, S. Li, J. Li, F. M. Peeters, and J. Wu, Nat. Commun. **5**, 3252 (2014).
[14] Z. Chi, X. Chen, F. Yen, F. Peng, Y. Zhou, J. Zhu, Y. Zhang, X. Liu, C. Lin, S. Chu, Y. Li, J. Zhao, T. Kagayama, Y. Ma, and Z. Yang, Phys. Rev. Lett. **120**, 037002 (2018).
[15] D. Biswas, A. M. Ganose, R. Yano, J. M. Riley, L. Bawden, O. J. Clark, J. Feng, L. Collins-Mcintyre, M. T. Sajjad, W. Meevasana, T. K. Kim, M. Hoesch, J. E. Rault, T. Sasagawa, D. O. Scanlon, and P. D. C. King, Phys. Rev. B **96**, 085205 (2017).
[16] D. A. Chenet, O. B. Aslan, P. Y. Huang, C. Fan, A. M. Van Der Zande, T. F. Heinz, and J. C. Hone, Nano Lett. **15**, 5667 (2015).
[17] E. Liu, Y. Fu, Y. Wang, Y. Feng, H. Liu, X. Wan, W. Zhou, B. Wang, L. Shao, C.-h. Ho, Y.-s. Huang, Z. Cao, L. Wang, A. Li, J. Zeng, F. Song, X. Wang, Y. Shi, H. Yuan, H. Y. Hwang *et al.*, Nat. Commun. **6**, 6991 (2015).
[18] D. Ghoshal, A. Yoshimura, T. Gupta, A. House, S. Basu, Y. Chen, T. Wang, Y. Yang, W. Shou, J. A. Hachtel, J. C. Idrobo, T. M. Lu, S. Basuray, V. Meunier, S. F. Shi, and N. Koratkar, Adv. Funct. Mater. **28**, 1801286 (2018).
[19] O. B. Aslan, D. A. Chenet, A. M. van der Zande, J. C. Hone, and T. F. Heinz, ACS Photon. **3**, 96 (2016).
[20] I. Gutiérrez-Lezama, B. A. Reddy, N. Ubrig, and A. F. Morpurgo, 2D Mater. **3**, 045016 (2016).
[21] S. M. Gunasekera, D. Wolverson, L. S. Hart, and M. Muchakruczynski, J. Electron. Mater. **47**, 4314 (2018).
[22] J. P. Echeverry and I. C. Gerber, Phys. Rev. B **97**, 075123 (2018).
[23] Y. Yan, C. Jin, J. Wang, T. Qin, F. Li, K. Wang, Y. Han, and C. Gao, J. Phys. Chem. Lett. **8**, 3648 (2017).
[24] J. E. Proctor, E. Gregoryanz, K. S. Novoselov, M. Lotya, J. N. Coleman, and M. P. Halsall, Phys. Rev. B **80**, 073408 (2009).
[25] Z.-H. Chi, X.-M. Zhao, H. Zhang, A. F. Goncharov, S. S. Lobanov, T. Kagayama, M. Sakata, and X.-J. Chen, Phys. Rev. Lett. **113**, 036802 (2014).
[26] A. P. Nayak, Z. Yuan, B. Cao, J. Liu, J. Wu, S. T. Moran, T. Li, D. Akinwande, C. Jin, and J.-F. Lin, ACS Nano **9**, 9117 (2015).
[27] S. N. Gupta, A. Singh, K. Pal, B. Chakraborty, D. V. S. Muthu, U. V. Waghmare, and A. K. Sood, Phys. Rev. B **96**, 094104 (2017).
[28] T. Sasaki, K. Kondo, Y. Akahama, S. Nakano, and T. Taniguchi, Jpn. J. Appl. Phys. **56**, 05FB06 (2017).
[29] A. P. Nayak, S. Bhattacharyya, J. Zhu, J. Liu, X. Wu, T. Pandey, C. Jin, A. K. Singh, D. Akinwande, and J.-F. Lin, Nat. Commun. **5**, 3731 (2014).

[30] Z. Zhao, H. Zhang, H. Yuan, S. Wang, Y. Lin, Q. Zeng, G. Xu, Z. Liu, G. K. Solanki, K. D. Patel, Y. Cui, H. Y. Hwang, and W. L. Mao, Nat. Commun. **6**, 7312 (2015).

[31] S. Duwal and C.-S. Yoo, J. Phys. Chem. C **120**, 5101 (2016).

[32] Y. Guo, H. Deng, X. Sun, X. Li, J. Zhao, J. Wu, W. Chu, S. Zhang, H. Pan, X. Zheng, X. Wu, C. Jin, C. Wu, and Y. Xie, Adv. Mater. **29**, 1700715 (2017).

[33] D. Zhou, Y. Zhou, C. Pu, X. Chen, P. Lu, X. Wang, C.-h. Ho, J. Sun, Z. Yang, and D. Xing, npj Quantum Mater. **2**, 19 (2017).

[34] P. Wang, Y. Wang, J. Qu, Q. Zhu, W. Yang, J. Zhu, L. Wang, W. Zhang, D. He, and Y. Zhao, Phys. Rev. B **97**, 235202 (2018).

[35] R. Oliva, M. Laurien, F. Dybala, J. Kopaczek, Y. Qin, S. Tongay, O. Rubel, and R. Kudrawiec, npj 2D Mater. Appl. **3**, 20 (2019).

[36] D. Hou, Y. Ma, J. Du, J. Yan, C. Ji, and H. Zhu, J. Phys. Chem. Solids **71**, 1571 (2010).

[37] L. Liang, J. Zhang, B. G. Sumpter, Q. H. Tan, P. H. Tan, and V. Meunier, ACS Nano **11**, 11777 (2017).

[38] Y. Feng, W. Zhou, Y. Wang, J. Zhou, E. Liu, Y. Fu, Z. Ni, X. Wu, H. Yuan, F. Miao, B. Wang, X. Wan, and D. Xing, Phys. Rev. B **92**, 054110 (2015).

[39] N. R. Pradhan, A. McCreary, D. Rhodes, Z. Lu, S. Feng, E. Manousakis, D. Smirnov, R. Namburu, M. Dubey, A. R. Hight Walker, H. Terrones, M. Terrones, V. Dobrosavljevic, and L. Balicas, Nano Lett. **15**, 8377 (2015).

[40] A. McCreary, J. R. Simpson, Y. Wang, D. Rhodes, K. Fujisawa, L. Balicas, M. Dubey, V. H. Crespi, M. Terrones, and A. R. Hight Walker, Nano Lett. **17**, 5897 (2017).

[41] W. Kohn and L. J. Sham, Phys. Rev. **140**, A1133 (1965).

[42] G. Kresse and J. Furthmüller, Phys. Rev. B **54**, 11169 (1996).

[43] G. Kresse and D. Joubert, Phys. Rev. B **59**, 1758 (1999).

[44] P. E. Blöchl, Phys. Rev. B **50**, 17953 (1994).

[45] J. P. Perdew, K. Burke, and M. Ernzerhof, Phys. Rev. Lett. **77**, 3865 (1996).

[46] J. Klimeš, D. R. Bowler, and A. Michaelides, J. Phys.: Condens. Matter **22**, 022201 (2010).

[47] J. Klimeš, D. R. Bowler, and A. Michaelides, Phys. Rev. B **83**, 195131 (2011).

[48] J. Sun, A. Ruzsinszky, and J. P. Perdew, Phys. Rev. Lett. **115**, 036402 (2015).

[49] J. C. Wildervanck and F. Jellinek, J. Less-Common Met. **24**, 73 (1971).

[50] See Supplemental Material at http://link.aps.org/supplemental/10.1103/PhysRevB.100.214101 for a comparison of lattice parameters obtained with different functionals and experimental results, additional information on electronic and vibrational properties, and technical details of Raman intensity calculations.

[51] F. D. Murnaghan, Am. J. Math. **59**, 235 (1937).

[52] F. Birch, Phys. Rev. **71**, 809 (1947).

[53] A. Togo and I. Tanaka, Scr. Mater. **108**, 1 (2015).

[54] S. Baroni, S. D. Gironcoli, A. D. Corso, and P. Giannozzi, Rev. Mod. Phys. **73**, 515 (2001).

[55] P. Pavone, K. Karch, O. Schutt, W. Windl, D. Strauch, P. Giannozzi, and S. Baroni, Phys. Rev. B **48**, 3156 (1993).

[56] N. Mounet and N. Marzari, Phys. Rev. B **71**, 205214 (2005).

[57] D. Tristant, A. Cupo, and V. Meunier, 2D Mater. **5**, 035044 (2018).

[58] D. Tristant, A. Cupo, X. Ling, and V. Meunier, ACS Nano **13**, 10456 (2019).

[59] L. Liang and V. Meunier, Nanoscale **6**, 5394 (2014).

[60] A. Molina-Sánchez, M. Palummo, A. Marini, and L. Wirtz, Phys. Rev. B **93**, 155435 (2016).

[61] H. P. C. Miranda, S. Reichardt, G. Froehlicher, A. Molina-Sánchez, S. Berciaud, and L. Wirtz, Nano Lett. **17**, 2381 (2017).

[62] M. Shishkin and G. Kresse, Phys. Rev. B **74**, 035101 (2006).

[63] M. Rahman, K. Davey, and S. Z. Qiao, Adv. Funct. Mater. **27**, 1606129 (2017).

[64] M. Samadi, N. Sarikhani, M. Zirak, H. Zhang, H. L. Zhang, and A. Z. Moshfegh, Nanoscale Horiz. **3**, 90 (2018).

[65] N. Sheremetyeva, D. J. Cherniak, E. B. Watson, and V. Meunier, Phys. Chem. Miner. **45**, 173 (2018).

[66] A. Rohatgi, "Webplotdigitizer", https://automeris.io/WebPlotDigitizer, 2019.

[67] X. Zhang, Q.-H. Tan, J.-B. Wu, W. Shi, and P.-H. Tan, Nanoscale **8**, 6435 (2016).

[68] G. Dolling and B. N. Brockhouse, Phys. Rev. **128**, 1120 (1962).

[69] R. Nicklow, N. Wakabayashi, and H. G. Smith, Phys. Rev. B **5**, 4951 (1972).

[70] J. Serrano, A. Bosak, R. Arenal, M. Krisch, K. Watanabe, T. Taniguchi, H. Kanda, A. Rubio, and L. Wirtz, Phys. Rev. Lett. **98**, 095503 (2007).

[71] N. Wakabayashi, H. Smith, and R. Nicklow, Phys. Rev. B **12**, 659 (1975).

[72] H. Tornatzky, R. Gillen, H. Uchiyama, and J. Maultzsch, Phys. Rev. B **99**, 144309 (2019).

[73] Y. Fujii, Y. Akahama, S. Endo, S. Narita, Y. Yamada, and G. Shirane, Solid State Commun. **44**, 579 (1982).

[74] Y. Yamada, Y. Fujii, Y. Akahama, S. Endo, S. Narita, J. D. Axe, and D. B. McWhan, Phys. Rev. B **30**, 2410 (1984).

[75] S. Curtarolo, W. Setyawan, G. L. Hart, M. Jahnatek, R. V. Chepulskii, R. H. Taylor, S. Wang, J. Xue, K. Yang, O. Levy *et al.*, Comput. Mater. Sci. **58**, 218 (2012).

[76] X.-F. Qiao, J.-B. Wu, L. Zhou, J. Qiao, W. Shi, T. Chen, X. Zhang, J. Zhang, W. Ji, and P.-H. Tan, Nanoscale **8**, 8324 (2016).

[77] Y. Wang, B. R. Carvalho, and V. H. Crespi, Phys. Rev. B **98**, 161405(R) (2018).